Journal of Alloys and Compounds 509 (2011) 1493–1500

Contents lists available at ScienceDirect

Journal of Alloys and Compounds

journal homepage: www.elsevier.com/locate/jallcom

Dense $La_{0.9}Sr_{0.1}Ga_{0.8}Mg_{0.2}O_{2.85}$ electrolyte for IT-SOFC's: Sintering study and electrochemical characterization

K. Traina [a,*], C. Henrist [b], B. Vertruyen [c], R. Cloots [a]

[a] Group of Research in Energy and ENvironment from MATerials (GREEnMat), Chemistry Institute B6a, University of Liège, Sart-Tilman, B-4000 Liège, Belgium
[b] Center for Applied Technology of Microscopy (CATμ), Chemistry Institute B6a, University of Liège, Sart-Tilman, B-4000 Liège, Belgium
[c] Laboratory of Structural Inorganic Chemistry (LCIS), Chemistry Institute B6a, University of Liège, Sart-Tilman, B-4000 Liège, Belgium

ARTICLE INFO

Article history:
Received 29 July 2010
Received in revised form 11 October 2010
Accepted 22 October 2010
Available online 4 November 2010

Keywords:
Substituted lanthanum gallate
Electrochemical impedance spectroscopy
Dielectric response
Grain boundaries
Ionic conduction
Microstructure

ABSTRACT

This paper presents the sintering behaviour of a $La_{0.9}Sr_{0.1}Ga_{0.8}Mg_{0.2}O_{2.85}$ coral-like microstructure powder. This is prepared by a successive freeze-drying and self-ignition process followed by calcination at 1200 °C during 1 h. This synthesis method gives great uniformity of the powder and allows shaping into compacts without requiring a grinding step. The grain size distribution (between 0.5 and 4 μm) favours a good sintering behaviour: open porosity disappear at 1400 °C and relative densities over 99% can be achieved after 6 h at 1450 °C. The same powder can also be sintered into a thin disc of ~100 μm thickness. The characterization of the dense material by impedance spectroscopy shows that the activation energies below and above 600 °C are 1.0 eV and 0.7 eV, respectively. The conductivity at 800 °C is ~0.11 S cm^{-1}. Special attention is devoted to the temperature range between 200 °C and 400 °C, where the intragrain and intergrain contributions can be distinguished. The analysis of the parameters describing the intragrain constant phase element in the equivalent circuit suggests that, above 325 °C, the system evolves from a distribution of relaxation time to only one relaxation time. The analysis of the data by the complexes permittivity show that ionic oxide conduction mechanism would occur in two steps. In the first, an oxygen vacancy would be released and, in the second, the migration of the ionic oxide would take place in the material.

1. Introduction

Because of their good ionic conductivity in the intermediate temperature range (500–800 °C), substituted lanthanum gallate compounds such as $La_{0.9}Sr_{0.1}Ga_{0.8}Mg_{0.2}O_{2.85}$ (abbreviated LSGM12 in the follow) are potential candidates to replace yttrium stabilized zirconia (YSZ) as electrolyte in solid oxide fuel cells [1,2]. However, in addition to having good electric properties, the solid-state electrolyte must have a very low closed porosity and no open porosity also in order to limit the resistance constraints or decrease the efficiency of the cell. This state depends essentially on the grain size distribution of the starting powder during the manufacturing process. Indeed, too small granulometry tends to promote grain growth and coarsening to the detriment of densification, whereas large granulometry results in big porosity and excessive sintering time. In addition, defects trapped in the green body (voids) usually persist in the sintered material [3,4]. Many authors have tried to optimize the synthesis conditions of LSGM12 powders in order to achieve low porosity in the final material. However, whatever the synthesis method (solid-state reaction [5–8], Pechini method [9–11], acrylamide polymerisation [12] or glycine nitrate combustion [13,14]), the powders need to be ground before shaping and only a few papers report the grain size distribution [15–21] after this step.

In a previous paper [22], we reported the synthesis and the detailed microstructural characterizations of powder with coral-like microstructure prepared by a successive freeze-drying and self-ignition process. When that powder is lightly pressed (25 MPa) into a compact (without any prior grinding step), the coral-like microstructure collapses and results in a very narrow particle size distribution in the 0.5–4 μm range. The objective of the present paper is to study the densification behaviour of that powder. Since very high relative density (up to 99.3%, amongst the best results in literature [6,23–26]) can be obtained, we also characterize the electrical properties by impedance spectroscopy. It is well known [27] that excessive residual porosity may lead to interpretation problems, especially concerning the intermediate frequency arcs generally attributed to grain boundary effects: a high relative density helps to minimize the artefacts caused by microstructural defects.

2. Materials and methods

LSGM12 powder was prepared by a method combining freeze-drying and self-ignition of an aqueous solution containing metallic nitrates and hydroxypropy-

* Corresponding author. Tel.: +32 4 366 3532; fax: +32 4 366 3413.
E-mail address: karl.traina@ulg.ac.be (K. Traina).

0925-8388/$ – see front matter © 2010 Elsevier B.V. All rights reserved.
doi:10.1016/j.jallcom.2010.10.117

lmethyl cellulose [22]. To obtain a powder with good sinterability properties, LSGM12 powder was prepared in two steps in this study. In the first, the intermediate powder obtained after the self-ignition is calcined at 560 °C during 6 h to remove the residual carbon. In the second, the as-powders are thermally treated at 1200 °C during 1 h to obtain the perovskite structure. For all thermal treatments, the heat rate is 5 °C/min. Powders are furnace cooled to room temperature. Then, the powder calcined at 1200 °C was submitted to 25 MPa uniaxial pressure to shape a disc (0.5 mm in thickness and 5 mm in diameter) before dispersion into water by sonication for 30 s (Transsonic TS 540 Elma, 35 kHz–77 W). The grain size distribution measurement was performed with a Malvern – Mastersizer 2000 – Hydro 2000S apparatus. Scanning electron microscopy (Philips ESEM XL30 FEG) was used to observe the morphology and particle size of powders and fractured surfaces. All powders were characterized by X-ray diffraction (Siemens D5000 powder diffractometer, CuK_α – not shown here).

For the densification study, green compacts were shaped into ~5 mm diameter cylinders by uniaxial pressing (50 MPa) before compressing isostatically at 220 MPa. For all green samples, compactness estimated from mass and geometrical dimensions (diameter and height of cylinders) is close to 56%. Linear shrinkage was measured in an Adamel D124 dilatometer: a green cylinder was heated under air until 1450 °C during 2 h. The heating and cooling rates are both 5 °C/min. In order to characterize the microstructure evolution during the densification process, some cylinders were sintered at 1100 °C, 1200 °C, 1300 °C, 1400 °C and 1450 °C. The density of the sintered cylinders was measured by Archimedes method in 2-butanol using a Mettler Toledo kit. From these data, the open and closed porosity were calculated.

In order to express the relative value of the cohesion forces between the sintered grains, microhardness Vickers measurements (Instron Wilson – Wolpert Tukon® 2100B) were conducted: the imprints on the cylinders surface were measured after applying 1 kg during 10 s. Surfaces were not post-processed (polishing, metallization. . .). Brown and black cylinders were then fractured and observed by scanning electron microscopy (Philips ESEM XL30 FEG). To reveal the grain boundaries, a last cylinder sintered at 1450 °C during 6 h was polished by SiC paper (220 to 4000 mesh) and thermally etched at 1350 °C during 1 h.

A very thin disc was prepared in order to demonstrate the ability to prepare thin films such as used for the manufacture of electrolyte-supported SOFC [28]. 50 mg of the LSGM12 powder were placed in a mould of 13 mm in diameter. In order to minimize adhesion to the mould, a few millilitres of petroleum ether (60–40) were added. Uniaxial compression (7 MPa) expelled the liquid and the green disc was shaped. The disc was then transferred on a rigid platinum sheet and sintered at 1450 °C during 1 h with 5 °C/min heating and cooling rate. The disc was characterized by scanning electron microscopy (Philips ESEM XL30 FEG). Its density after thermal treatment was measured by Archimedes method in 2-butanol by a Berman balance [29].

To characterize the electrical properties, a green disc of ~13 mm in diameter was prepared in the same pressure conditions as cylinders. The disc was heated at 5 °C/min to 1450 °C and sintered in air during 6 h. The black disc was then furnace cooled to room temperature. The final diameter and thickness were 9.97 and 2.86 ± 0.01 mm, respectively. The density was measured by Archimedes method. The planar opposite surfaces of the disc were painted with SPI® Supplies Pt paste and fired at 1000 °C before cooling at room temperature. The cell was positioned inside a tubular furnace. Impedance diagrams were obtained with a computer-controlled Solartron 1260 impedance analyzer with a 500 mV amplitude signal over the frequency range 4×10^{-3} Hz–12 MHz under 400 °C and between 0.01 Hz and 12 MHz at higher temperature.

3. Results and discussion

3.1. Densification

A micrograph of the LSGM12 powder used as starting material for the densification study is shown in Fig. 1. Particles are connected in a coral-like microstructure. Fig. 2a shows the micrograph of a green fractured disc compacted at light pressure (25 MPa) with this powder. The resulted individual grains seem rather uniform and monodisperse. Fig. 2b shows the volume (grey histogram) and numerical (white histogram) grain size distribution obtained after the dispersion of the compacted disc in water by an ultrasonic probe. The descriptors of these distributions are shown in Table 1. We can see that the width of these distributions is narrow (span is close to the unity) and their ranges are very close. These data confirm clearly the monodisperse behaviour of the collapsed powder. Therefore, this started LSGM12 powder can be shaped into discs without needing a grinding step and avoids all potential sources of contaminant.

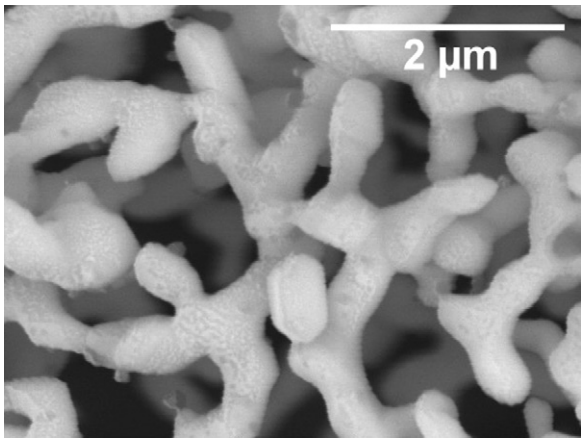

Fig. 1. Electron micrograph of the LSGM12 powder obtained after self-ignition and calcination at 1200 °C during 1 h.

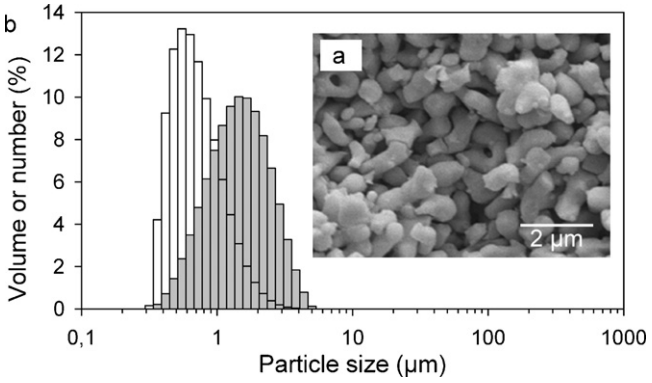

Fig. 2. (a) Electron micrograph of green disc fractured after shape forming. (b) Volume (grey histogram) and numerical (white histogram) grain size distributions obtained after dispersion of the green disc in water by an ultrasonic probe.

Fig. 3a displays the shrinkage curve obtained when heating a green cylinder up to 1450 °C in air. Shrinkage starts at ~840 °C and progresses up to the maximum temperature. The densification is further improved by a 2 h dwell at 1450 °C. The final shrinkage percentage is 25.8%. Fig. 3b shows the open and closed porosities measured by Archimedes method at experimental conditions corresponding to the points marked by circles on the shrinkage curve. Below 1400 °C, the open porosity decreases with increasing tem-

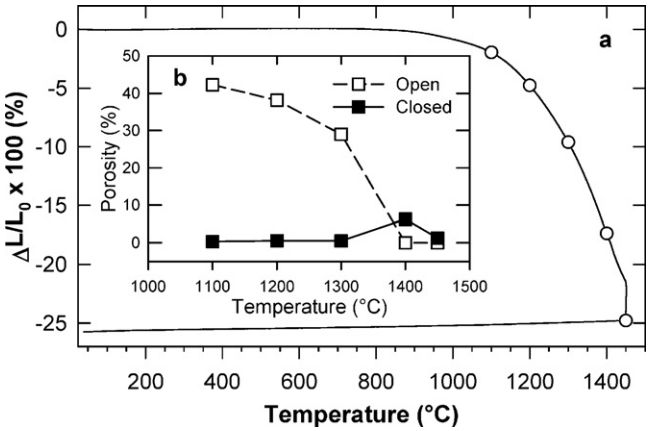

Fig. 3. (a) Shrinkage curve of a green cylinder heated to 1450 °C. (b) Open and closed porosity of cylinders sintered with experimental conditions corresponding to the points marked by circles in the shrinkage curve.

Table 1
Volume and numerical grain size distribution descriptors for the LSGM12 starting material calcined at 1200 °C during 1 h.

	$d_{0.1}$ (μm)	$d_{0.5}$ (μm)	$d_{0.9}$ (μm)	Mode (μm)	Span, $(d_{0.9} - d_{0.1})/d_{0.5}$
Volume grain size distribution	0.61	1.14	2.08	1.16	1.29
Number grain size distribution	0.40	0.60	1.07	0.54	1.12

perature while the closed porosity remains close to zero. At 1400 °C, the open porosity becomes zero and the closed porosity increases indicating the closure of the external surface of the cylinder and the trapping of the previous open porosity. At higher temperature, part of closed porosity is eliminated. The residual porosity after 2 h sintering at 1450 °C is 1.3%. Increasing the duration of the sintering to 6 h does not lead to a detectable change of the porosity (not shown here).

To illustrate the densification process, Fig. 4a–c shows electron micrographs of fractured cylinders sintered at 1200 °C, 1300 °C and 1400 °C. Besides, microhardness Vickers measurements (Fig. 4d) were conducted in order to express the relative value of the intergranular cohesion forces. Note that only hardnesses of the cylinders sintered between 1200 °C and 1400 °C could be measured. Below this temperature range, the cylinders are still too friable and above, the cylinders become too hard: the imprints show ductile transition and hardness values become erroneous. So, these results indicate that the coalescence begins around 1200 °C (Fig. 4a). Below this temperature, the shrinkage probably corresponds to a reorganisation of the material. From 1200 °C to 1400 °C (Fig. 4b and c), the granular cohesion increases. At higher temperature, the material is dense and the cohesion is stronger.

Final microstructure of the black cylinder sintered at 1450 °C during 6 h is shown in Fig. 5a. Fig. 5a shows the electron micrograph of the fractured cylinder and Fig. 5b shows the electron backscattered micrograph of the black cylinder polished and thermally etched. Both show that the pores seem to be homogenously distributed and are mainly localised at the grain corners [4] (see Fig. 5b). The size of the grains ranges between 1 and 10 μm and no abnormal distribution is observed. Scanning electron microscopy does not reveal any secondary phase. This confirms our previous XRD results [22] that showed that the small amount of $LaSrGaO_4$ impurity in the powder calcined at 1200 °C disappears upon thermal treatment at higher temperature.

Fig. 6 shows micrographs of a thin disc obtained by the procedure described as before (see Section 2). The disc thickness is 107 μm. The pore distribution appears rather homogeneous (see Fig. 6a). The pore size is slightly bigger than for the isostatically pressed cylinders. The disc surface (Fig. 6b) shows grain size ranging between 1 and 5 μm and some pinholes localised at grain boundaries and grain corners. In addition, the density measurement (by the Archimedes method using a Berman balance) confirms that the disc does not have open porosity. The relative density is 98 ± 2%. Although our equipment is not optimized to press very thin pellets, these observations show that it is possible to obtain a thin disc free from open porosity.

These results are encouraging and show that LSGM12 powders prepared by the method combining freeze-drying and self-ignition can be used to obtain dense electrolyte material without any grinding step which may introduce some contaminants. The densification study shows that the LSGM12 powder calcined at 1200 °C during 1 h displays very good sinterability properties and should be suitable to prepare thin discs or films [20,21,26] for the manufacture of electrolyte-supported SOFC [28].

3.2. Electrochemical characterization

Usually, the electrical properties of solid ionic conductor material is temperature depending. These properties may be studied by Electrochemical Impedance Spectroscopy (EIS) [30–38]. However, the frequency and resistive limits of the instrumentation do not make it possible to detect and deconvoluate in once all the electrochemical processes present. So, at room temperature, the resistance of an oxide ion electrolyte material is large (>1 MΩ) and this one behaves like a dielectric. In the intermediate temperatures range (200–400 °C), the contributions intragrains and intergrains may be observed in their entirety but not those relating to the electrodes. These lasts may be analysed at higher temperatures (>400 °C) [30,39,40].

Therefore, the electrical properties characterization was performed on a disc sintered at 1450 °C during 6 h. The final diameter and thickness are 9.97 mm and 2.86 mm, respectively. The relative density is 99.3%. Fig. 7 shows the impedance diagrams recorded at 237 °C, 398 °C and 600 °C. They are respectively representative of the behaviours observed in the intermediate temperatures range and above: between 200 °C and 325 °C; between 325 °C and 400 °C and finally above 400 °C. By convention, numbers given above the experimental points refer to the decade exponent of the frequency. Fig. 7a shows that simultaneously the high and intermediary frequency arcs corresponding respectively to intragrain and intergrain behaviours can be observed. Fig. 7b shows that an inductive contribution appears: the high frequency arc becomes distorted and the diagram does not intercept the origin any more. The contribution of electrode electrochemical processes in the low frequency range becomes increasingly noticeable when the temperature rises. Finally, when the temperature becomes higher than 500 °C (see Fig. 7c recorded at 600 °C), the capacitive contributions of the material disappear and only its total resistivity can be measured (as the intersection of the diagram with the Z' axis).

The equivalent circuits used to fit the normalized experimental data are also shown in Fig. 7: R_g and R_{ig} are respectively the intragrain and intergrain resistivity; CPE_g and CPE_{ig} are constant phase elements describing the capacitive behaviour; $A_{(i)g}$ and $\alpha_{(i)g}$ are parameters which define the impedance of the constant phase element CPE and L is the inductance observed when the temperature increases. Table 2 presents the fitted parameters associated to the resistive and capacitive circuit components between 200 °C and 400 °C.

The intergrain contribution to the total resistivity is given by the R_{ig}/R_{tot} ratio (also known as blocking factor α_R [41]). In the case of stabilized zirconia (YSZ), it has been shown that α_R becomes zero around 730 °C [41]. In the present case (LSGM12), α_R does not vary significantly in the temperature range (200–400 °C) where the inductive component permits the distinction between the intragrain and intergrain contributions. This was also observed by Iguchi et al. [42] in their work on $La_{0.8}Sr_{0.2}GaO_{3-\delta}$. As a result, we cannot assume that the total resistivity is equal to the intragrain resistivity in the high temperature range (>400 °C). Consequently, Fig. 8 shows two Arrhenius plots: one with intragrain resistivity data (R_g) between 200 °C and 400 °C and the other one with total resistivity data (R_{tot}) in the whole temperature range (200–1000 °C). Actually, below 400 °C the activation energy E_g associated to the intragrain conduction mechanism is very close to that associated to the total resistivity. The activation energy values E_1 and E_2 below and above 600 °C respectively and the conductivity at 800 °C are compared with literature data for the same composition in Table 3. Except for one paper reporting data in a narrow temperature range [45], our data confirm the results found by other authors. The higher

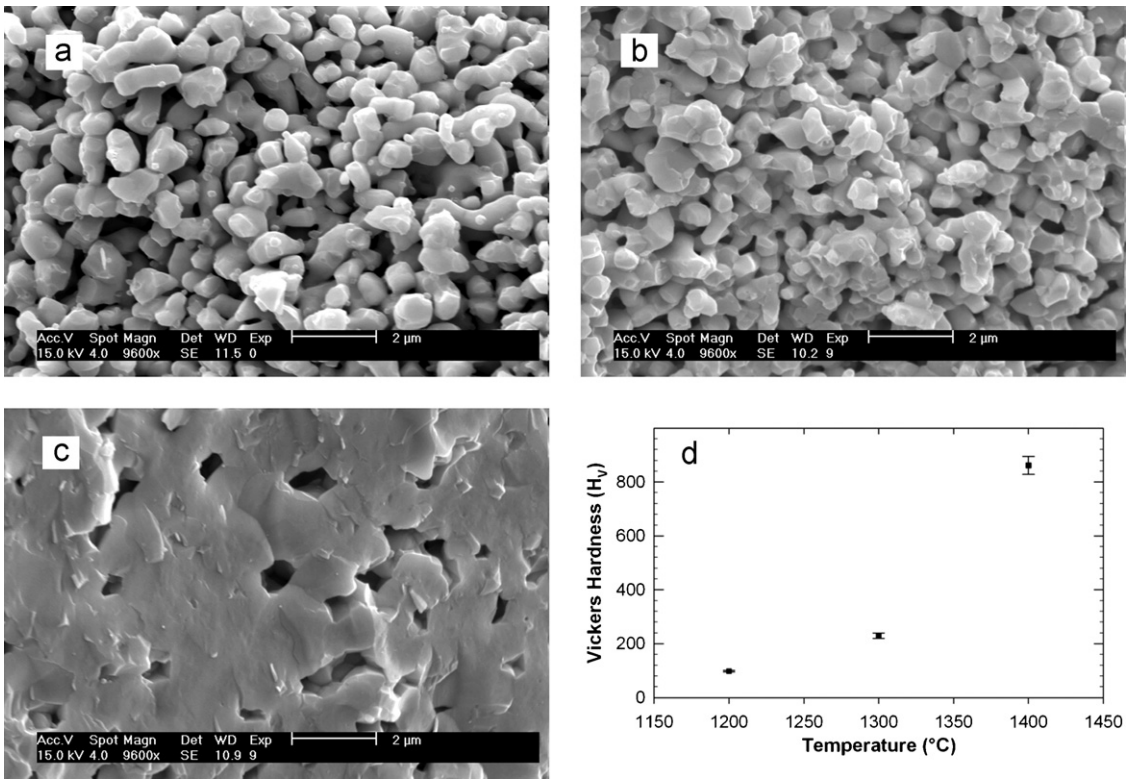

Fig. 4. Electron micrographs for cylinders sintered at (a) 1200 °C, (b) 1300 °C and (c) 1400 °C. (d) Corresponding Vickers microhardness values.

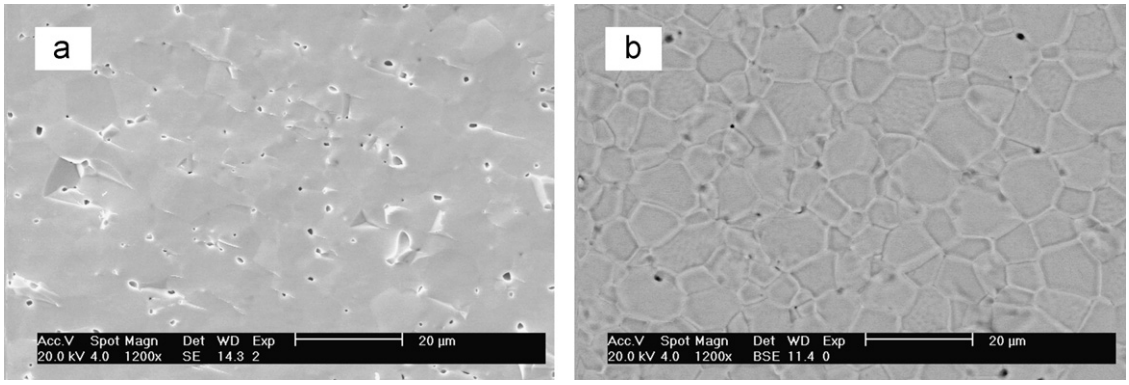

Fig. 5. Electron micrographs of the cylinders sintered at 1450 °C during 6 h: (a) unpolished fracture (secondary electrons) and (b) polished fracture thermally etched at 1350 °C during 1 h (back-scattered electrons).

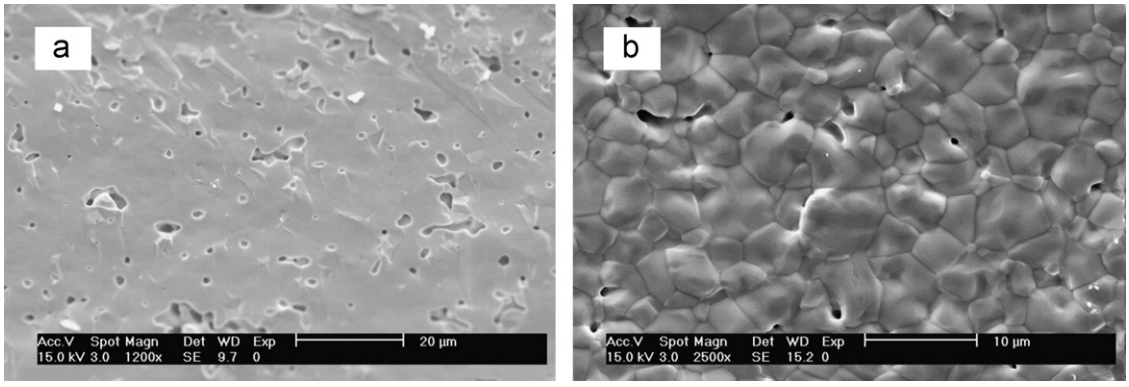

Fig. 6. Electron micrographs of a thin disc obtained by the procedure described in the Material and methods section: (a) unpolished cross-section and (b) disc surface.

Table 2
Impedance diagram fit parameters. The subscripts 'g' and 'ig' correspond to intragrain and intergrain parameters. R stands for resistivity, A and α define the impedance of a CPE where $Z_{CPE} = (1/A)(j\omega)^{-\alpha}$. The permittivity C is calculated as $(A \cdot R^{1-\alpha})^{1/\alpha}$. R_{ig}/R_{tot} is the blocking factor α_R, where R_{tot} is the total resistivity.

T (°C)	R_g (Ω m)	A_g, $\times 10^9$ ($S\,m^{-1}\,s^{\alpha}$)	α_g	C_g, $\times 10^{10}$ (F/m)	R_{ig} (Ω m)	A_{ig}, $\times 10^5$ ($S\,m^{-1}\,s^{\alpha}$)	α_{ig}	C_{ig}, $\times 10^6$ (F/m)	$\alpha_R = R_{ig}/R_{tot}$, $\times 100$ (%)
200	18,900	2.7	0.86	5.8 ± 0.3	5300	0.6	0.65	1.0 ± 0.8	28.0
237	3640	4.0	0.85	5.9 ± 0.2	965	1.2	0.66	1.2 ± 0.6	26.5
284	610	4.7	0.86	6.0 ± 0.3	161	2.7	0.64	1.3 ± 0.8	26.5
328	144	5.5	0.86	6.0 ± 0.3	37.9	5.1	0.63	1.4 ± 0.8	26.3
368	47.1	3.7	0.90	6.6 ± 1.0	13.1	7.4	0.63	1.3 ± 0.8	27.8
398	19.1	1.3	0.98	8.6 ± 0.9	6	13.0	0.59	1.0 ± 0.4	31.4

activation energy observed at low temperature is likely due to trapping of oxygen vacancies at low temperature. This is a classical behaviour for ionic conductors; it is observed for scandia doped zirconia [47,48] and for bismuth based oxide ion conductors, namely BIMEVOX compounds, [49–51] too.

Although the analysis of impedance diagrams often focuses only on the resistive components, it is also interesting to observe the dependence of the capacitive component as a function of temperature. The intragrain permittivity (C_g) was calculated by the equation [52]:

$$C_g = (A_g \cdot R_g^{1-\alpha_g})^{1/\alpha_g} \quad (1)$$

where C_g and R_g are the intragrain permittivity and resistivity, respectively; A_g and α_g define the impedance of a CPE where $Z_{CPE} = (1/A)(j\omega)^{-\alpha}$. As can be seen in Table 2 for 200 °C < T < 400 °C, C_g does not vary significantly below 325 °C but increases at higher temperature. Since A_g and R_g decrease between 325 °C and 400 °C, it can be concluded from Eq. (1) that the increase of C_g results from the increase of the α_g parameter. The fact that α_g approaches 1 suggests that the circuit component evolves from a CPE behaviour (characterized by a distribution of relaxation times) to a simple capacitor (characterized by only one relaxation time). Such a modification of equivalent circuit component characteristics is expected to correspond to a variation of some properties of the material as discussed hereafter.

It is usually considered that all cations in $La_{0.9}Sr_{0.1}Ga_{0.8}Mg_{0.2}O_{2.85}$ are statistically distributed on the crystallographic sites. However, this is not the case in true samples, where local minor variations of composition are to be expected. Computer simulations carried out by Islam and Davies [53] have predicted that association of oxygen vacancies with magnesium at nearest-neighbour sites (as trimers $Mg'_{Ga}\ V_O^{\cdot\cdot}\ Mg'_{Ga}$ using the Kröger-Vink notation [54]) is energetically favoured and that the stabilization energy depends on the size of the Mg-vacancies clusters. Therefore, any local inhomogeneity of the magnesium distribution in the material would correspond to local variations of the oxygen vacancy transport, resulting in a distribution of relaxation times. When the temperature increases, the oxygen vacancies are less likely to be trapped by magnesium ions. So, as the oxide ions O^{2-} is migrating more easily, as the intergrain resistivity is decreasing. The system appears electrically as more homogeneous.

In addition, we can see that the α_g parameter in this study (see in Table 2) is smaller than one's obtained by Kurumada et al. [55] for the composition $La_{0.9}Sr_{0.1}Ga_{0.9}Mg_{0.1}O_{2.9}$ in the temperature range between 200 °C and 380 °C: 0.93 ± 0.01. This difference probably comes from the content of substituted cations, higher for the $La_{0.9}Sr_{0.1}Ga_{0.8}Mg_{0.2}O_{2.85}$ composition. This content increases the number of ways of possible migration and undoubtedly makes the system electrically less "homogeneous".

Although Table 2 shows that C_{ig} seems to remain constant in the temperature range considered, the intergranular capacitive behaviour may be discussed. Indeed, the parameters analysis shows that simultaneously A_{ig} parameter increases at 400 °C whereas α_{ig} moves away from the unit. These observations seem to reveal that the "capacitive" weight of the constant phase element tends to be reduced in favour of the resistive weight ($\alpha = 1$ for a pure capacitance and $\alpha = 0$ for a pure resistance element). In other words, the capacitive component intergrains tends to change and would give place to a more "resistive" behaviour. Kurumada et al. [55] explain this behaviour change by the dipole moment of the ions located at the grain boundaries As they are not packed up in a way as dense as those present in the grains, the dipole moment caused by the ionic displacement induced by the migration of the anions O^{2-} to the grain boundaries must be bigger than that induces by the migrations inside the grains. Thus, these bigger dipole moments must bring more large dielectric losses. Consequently, as LSGM12 sintered disc contains any porosity, heterogeneity characterized by the decentring angle β_{ig} only come from the grains boundaries. As the grain boundaries seem to be free from any secondary phase (cf. Fig. 5b), this heterogeneity probably finds its source at an atomic scale packing near the grain boundaries.

As the electrical properties of an ionic conductor depend on resistive and capacitive contributions, the temperature dependence can also be analysed from the complex permittivity ε. This variable is related to the impedance by the following equations [37,56].

$$Z^* = Z' - jZ'' = \frac{1}{j\omega C_g \varepsilon^*} \quad (2)$$

$$\varepsilon^* = \varepsilon' - j\varepsilon'' \quad (3)$$

In the case of a dielectric material, the permittivity constant ε is the potentiality of material to oppose fixed charges to electric field. Thus, as the stored charges are big; as the permittivity becomes large.

Table 3
Comparison of activation energies and conductivities with literature data for other $La_{0.9}Sr_{0.1}Ga_{0.8}Mg_{0.2}O_{2.85}$ samples.

References	E_1 (eV)	E_2 (eV)	$T_{transition}$ (°C)	Temperature range (°C)	Total conductivity at 800 °C ($S\,cm^{-1}$)
This work	1.01	0.71	600	200 < T < 1000	0.111
[43]	1.12	0.87	600	–	0.104
[44]	1.07	0.98	600	–	0.132
[45]	–	1.34	650	650 < T < 800	0.052
[46]	1.13		–	300 < T < 850	0.121

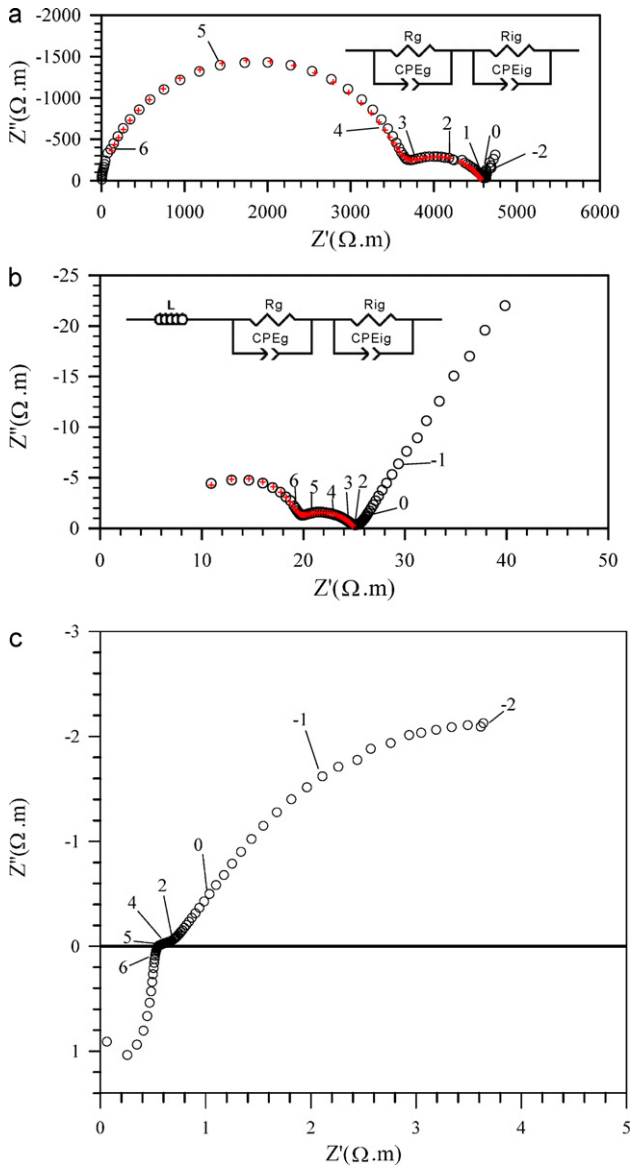

Fig. 7. Impedance diagrams recorded at (a) 297 °C, (b) 398 °C and (c) 600 °C. The numbers on the curves correspond to the decimal logarithm of the frequency expressed in Hertz. The crosses correspond to the result fitting of the equivalent circuits shown in the figure. The parameter values are presented in Table 2.

Moreover, the capacity of a condenser is expressed by:

$$C_g = \varepsilon \frac{S}{d} \tag{4}$$

where S is the surface area of the plates and d the distance between them. Thus, if the capacitance C_g is compared with the one of a condenser where the dielectric material is the vacuum, then, the value of the relative permittivity of the material ε_r can be calculated:

$$\frac{C_g}{C_0} = \frac{\varepsilon}{\varepsilon_0} = \varepsilon_r \tag{5}$$

However, as all dielectrics are not perfect, it is rather appropriated to give the relative permittivity in the complex plane:

$$\varepsilon_r = \varepsilon'_r - j\varepsilon''_r \tag{6}$$

where ε'_r is the real part of the relative permittivity whereas the imaginary part ε''_r is associated to the electric losses of the system. Henceforth, the losses in material can be calculated from ε'_r and ε''_r

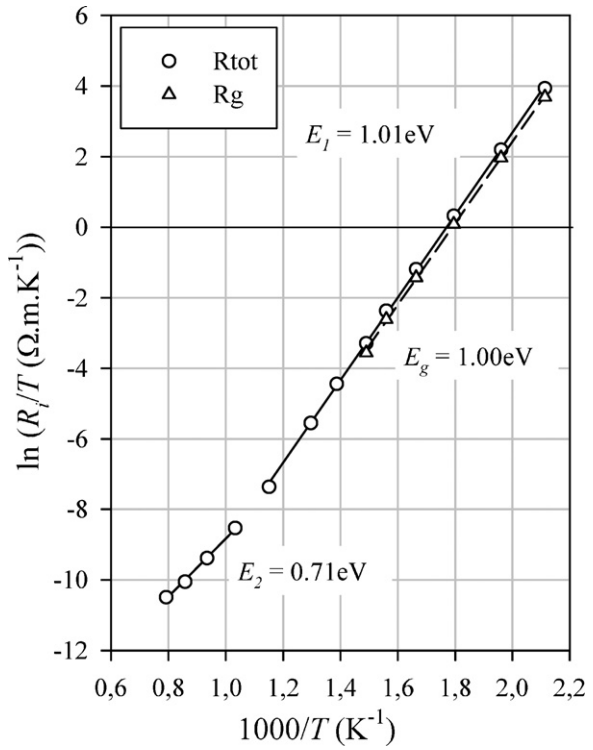

Fig. 8. Arrhenius plots ln(R/T) vs. 1000/T for intragrain resistivity data (R_g) between 200 °C and 400 °C and for total resistivity data (R_{tot}) between 200 °C and 1000 °C.

by:

$$\tan\delta = \frac{\varepsilon''_r}{\varepsilon'_r} \tag{7}$$

where $\tan\delta$ is called the loss angle tangent or the dielectric factor of dissipation. δ is the complementary angle to the phase shift observed between the tension applied to dielectric and the resulting current.

For dielectrics, the energy losses can be explained as follows [37]:

- at low frequencies, polarization follows the alternated field, its contribution to the permittivity is then maximum and the losses do not appear;
- at high frequencies, the field alternates too quickly and the material has not the time to adapt to this change. There is no component to the permittivity and no energy is lost in the medium;
- between these two opposite cases, the polarization is delayed compared to the electric field and part of energy is dissipated. The energy loss reaches a maximum value at a resonance frequency $f_{\tan\delta}$ given by $\tan\delta_{max}$.

In the case of the ionic conductor, activation energies E_M and E_D are related to $f_{\tan\delta}$ and $\tan\delta_{max}$ according to the next equations [42,55,57,58]:

$$f_{\tan\delta} \propto \exp\left(-\frac{E_M}{RT}\right) \tag{8}$$

and

$$T \cdot \tan\delta_{max} \propto \exp\left(-\frac{E_D}{RT}\right) \tag{9}$$

where E_M is the migration energy associated with the jump of an oxide ion O^{2-} between two different stable positions. Ionic displacement occurs around a saddle point along its diffusion pathway. E_D is the released energy of a vacancy $V_O^{\cdot\cdot}$ attached to a cluster.

Table 4
Activation energies for dielectric relaxing processes and electric conduction.

	E_M (eV)	E_D (eV)	$E_M + E_D$ (eV)	E_g (eV)
$La_{0.9}Sr_{0.1}Ga_{0.8}Mg_{0.2}O_{2.85}$ (this study)	0.96	0.06	1.02	1.00
$La_{0.8}Sr_{0.2}GaO_{2.9}$ [42]	0.96	0.13	1.09	0.99
$La_{0.9}Sr_{0.1}Ga_{0.1}Mg_{0.1}O_{2.9}$ [55]	0.94	0.05	0.99	0.99

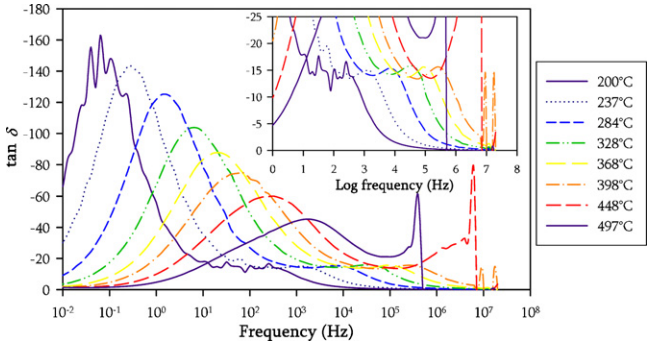

Fig. 9. (a) Dielectric factor of dissipation tan δ vs. the frequency f in logarithmic scale and (b) magnification on the high frequencies peak.

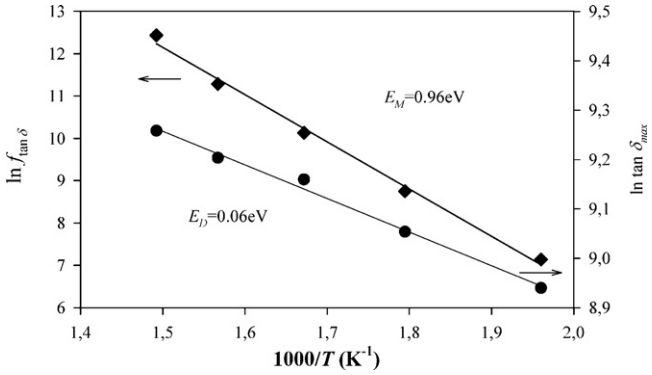

Fig. 10. Curves fit of $\ln f_{\tan\delta}$ and $\ln(T{\cdot}\tan\delta_{max})$ vs. $1/T$ for the high frequencies peaks and calculated activation energies. E_M and E_D are the ion oxide migration energy and released energy of a vacancy $V_O^{\cdot\cdot}$ attached to a cluster, respectively.

Therefore, graphs $\ln f_{\tan\delta}$ and $\ln(T{\cdot}\tan\delta_{max})$ vs. $1/T$ give the corresponding activation energies.

Fig. 9 shows the dielectric factor of dissipation tan δ vs. the frequency f recorded for various temperatures between 200 °C and 500 °C. A low and a high frequencies dielectric relaxation peaks are observed. Contrary to the dielectric relaxation processes occurred at low frequencies, the high frequencies processes can be observed only until 400 °C (see Fig. 9b). Moreover, whereas maximum dissipation tan δ_{max} of the low frequencies peak decreases with the temperature, the dissipation of the high frequencies peak seems to remain constant. Above this temperature range, no relaxation peak is observed.

Fig. 10 shows the results and the fitting of ln $f_{\tan\delta}$ and $\ln(T{\cdot}\tan\delta_{max})$ vs. $1/T$ for the high frequencies peaks. These peaks correspond to the intragranular contribution in the impedance plane. The estimated activations energies E_M and E_D, their sum and E_g are shown in Table 4.

So, around 2%, the activation energy of the electric conduction E_g would be equal to the sum of the migration energy E_M and the energy E_D of a mobile oxide ion vacancy O^{2-} [57]. The conduction mechanism in the material would occur in two steps. In the first, a vacancy attached to a cluster would be released and, in the second, the migration of the oxide ions O^{2-} would occur. These values seem to agree with those obtained for other compositions of substituted lanthanum gallates (see Table 4). Therefore, energy to the O^{2-} migration would be constant whereas the released energy for the vacancy would depend on the nature and the concentration of the substituted cations.

4. Conclusion

We have studied the sintering behaviour of $La_{0.9}Sr_{0.1}Ga_{0.8}Mg_{0.2}O_{2.85}$ green cylinders. These were prepared from a powder with coral-like microstructure obtained by a successive freeze-drying and self-ignition process followed by a calcination step at 1200 °C during 1 h. It appears that this powder can be shaped into compacts without requiring a grinding step. The grain size distribution (between 0.5 and 4 μm) favours a good sintering behaviour: relative densities over 99% have been achieved after 6 h at 1450 °C. The residual closed pores are mainly localised at the grain corners. The grain size ranges between 1 and 10 μm and no abnormal distribution is observed. In order to demonstrate that this powder can be used for the manufacture of electrolyte-supported SOFC, a 100 μm-thick dense pellet has also been prepared.

The electrical properties of the dense material have been characterized by impedance spectroscopy. The activation energies below and above 600 °C are 1.01 eV and 0.71 eV, respectively. The conductivity at 800 °C is ~0.11 S cm^{-1}. Between 200 °C and 400 °C, the intragrain and intergrain contribution can be distinguished and the ratio between intergrain resistivity and total resistivity does not vary significantly with temperature. Besides, the analysis of the parameters describing the intragrain constant phase element in the equivalent circuit suggests that, above 325 °C, the system evolves from a distribution of relaxation time to only one relaxation time. The analysis of the data by the complexes permittivity shows that the activation energy E_g of the conduction mechanism is equal to the sum between ionic oxide migration energy E_M and the released energy E_D of a vacancy $V_O^{\cdot\cdot}$ attached to a cluster. The ionic oxide conduction mechanism would occur in two steps. In the first, an oxygen vacancy would be released and, in the second, the migration of the ionic oxide would take place in the material.

Acknowledgements

The authors thank Dr. Ir. M.C. Steil from LEPMI (Grenoble, France) for the dilatometry measurements and useful discussion. BV thanks the Belgian Science Policy (Belgian State) for a postdoctoral fellowship under the Interuniversity Attraction Poles programme (INANOMAT - P6/17).

References

[1] P. Singh, N.Q. Minh, Int. J. Appl. Ceram. Technol. 1 (2004) 5–15.
[2] A. Weber, E. Ivers-Tiffée, J. Power Sources 127 (2004) 273–283.
[3] D. Bernache-Assollant, Chimie-physique du frittage, Hermes, Paris, 1993.
[4] M.N. Rahaman, Ceramic Processing and Sintering, Marcel Dekker, Basel, New York, 2003, pp. 1–875.
[5] J. Drennan, V. Zelizko, D. Hay, F.T. Ciacchi, S. Rajendran, S.P.S. Badwal, J. Mater. Chem. 7 (1997) 79–83.
[6] F. Chen, M. Liu, J. Solid State Electrochem. 3 (1998) 7–14.
[7] K. Yamaji, T. Horita, M. Ishikawa, N. Sakai, H. Yokokawa, Solid State Ionics 121 (1999) 217–224.
[8] A.M. Azad, L.F. Er, J. Alloys Compd. 306 (2000) 103–112.
[9] K. Huang, J.B. Goodenough, J. Solid State Chem. 136 (1998) 274–283.

[10] A.C. Tas, P. Majewski, F. Aldinger, J. Am. Ceram. Soc. 83 (2000) 2954–2960.
[11] P. Majewski, M. Rozumek, A.C. Tas, F. Aldinger, J. Electroceram. 8 (2002) 65–73.
[12] S. Zha, C.R. Xia, X. Fang, H.B. Wang, D. Peng, G.Y. Meng, Ceram. Int. 27 (2001) 649–654.
[13] D. Lybye, K. Nielsen, Solid State Ionics 167 (2004) 55–63.
[14] D. Lee, J.H. Han, Y. Chun, R.H. Song, D.R. Shin, J. Power Sources 166 (2007) 35–40.
[15] X.Q. Ma, H. Zhang, J. Dai, J. Roth, R. Hui, T.D. Xiao, D.E. Reisner, J. Therm. Spray Technol. 14 (2005) 61–66.
[16] B. Rambabu, S. Ghosh, W. Zhao, H. Jena, J. Power Sources 159 (2006) 21–28.
[17] Z. Bi, M. Cheng, Y.L. Dong, H. Wu, Y. She, B. Yi, Solid State Ionics 176 (2005) 655–661.
[18] M. Matsuda, O. Ohara, K. Murata, S. Ohara, T. Fukui, M. Miyake, Electrochem. Solid State Lett. 6 (2003) A140–A143.
[19] Y. Du, N.M. Sammes, J. Eur. Ceram. Soc. 21 (2001) 727–735.
[20] I. Natali Sora, R. Pelosato, A. Simone, L. Montanaro, F. Maglia, G. Chiodelli, Solid State Ionics 177 (2006) 1985–1989.
[21] M. Shi, Y.D. Xu, C. Wang, Y.P. Yuan, P. Majewski, F. Aldinger, J. Mater. Process. Technol. 169 (2005) 179–183.
[22] K. Traina, M.C. Steil, J.P. Pirard, C. Henrist, A. Rulmont, R. Cloots, B. Vertruyen, J. Eur. Ceram. Soc. 27 (2007) 3469–3474.
[23] J.W. Stevenson, T.J. Armstrong, D.E. McCready, L.R. Pederson, W.J. Weber, J. Electrochem. Soc. 144 (1997) 3613–3620.
[24] S.V. Kesapragada, S.B. Bhaduri, S. Bhaduri, P. Singh, J. Power Sources 124 (2003) 499–504.
[25] K. Huang, M. Feng, J.B. Goodenough, J. Am. Ceram. Soc. 79 (1996) 1100–1104.
[26] T. Fukui, S. Ohara, K. Murata, H. Yoshida, K. Miura, T. Inagaki, J. Power Sources 106 (2002) 142–145.
[27] M.P. Seabra, V.M. Ferreira, Mater. Res. Bull. 37 (2002) 255–262.
[28] R. Pelosato, I. Natali Sora, V. Ferrari, G. Dotelli, C.M. Mari, Solid State Ionics 175 (2004) 87–92.
[29] H. Berma, Am. Mineral. 24 (1939) 434–440.
[30] J.-D. Kim, G.-D. Kim, J.-W. Moon, Y.-I. Park, W.-H. Lee, K. Kobayashi, M. Nagai, C.-E. Kim, Solid State Ionics 143 (2001) 379–389.
[31] C.K. Lee, C.S. Ong, Solid State Ionics 1 (17) (1999) 301–310.
[32] N. Trofimenko, H. Ullmann, Solid State Ionics 118 (1999) 215–227.
[33] M.C. Steil, J. Fouletier, M. Kleitz, P. Labrune, J. Eur. Ceram. Soc. 19 (2000) 815–818.
[34] S.P.S. Badwal, J. Drennan, Sci. Ceram. Interfaces II (1994) 71–111.
[35] *EIS Theory*, 2007, pp. 1–31. http://www.gamry.com/App_Notes/EIS_Primer/EIS_Primer_2007.pdf.
[36] S.P. Jiang, J.G. Love, S.P.S. Badwal, Key Eng. Mater. 125/126 (1997) 81–132.
[37] J.R. MacDonald, Impedance Spectroscopy: Emphasizing Solid Materials and Systems, John Wileys & Sons, New York, Chichester, Brisbane, Toronto, Singapore, 1987.
[38] S.P.S. Badwal, J. Drennan, J. Mater. Sci. 22 (1987) 3231–3239.
[39] M.J. Verkerk, A.J. Burggraaf, J. Electrochem. Soc. 130 (1983) 78–84.
[40] D.I. Bronin, I.Y. Yaroslavtsev, H. Nafe, F. Aldinger, Electrochim. Acta 49 (2004) 2435–2441.
[41] L. Dessemond, R. Muccillo, M. Hénault, M. Kleitz, Appl. Phys. A 57 (1993) 57–60.
[42] E. Iguchi, S. Nakamura, F. Munakata, M. Kurumada, Y. Fujie, J. Appl. Phys. 93 (2003) 3662–3664.
[43] K. Huang, R.S. Tichy, J.B. Goodenough, J. Am. Ceram. Soc. 81 (1998) 2565–2575.
[44] M. Feng, J.B. Goodenough, Eur. J. Solid State Inorg. Chem. 31 (1994) 663–672.
[45] R. Polini, A. Pamio, E. Traversa, J. Eur. Ceram. Soc. 24 (2004) 1365–1370.
[46] P.N. Huang, A. Petric, J. Electrochem. Soc. 143 (1996) 1644–1648.
[47] J.T.S. Irvine, J.W.L. Dobson, T. Politova, S.G. Martin, A. Shenouda, Faraday Discussions 134 (2007) 41–49.
[48] M. Angeles-Rosas, M.A. Camacho-Lopez, E. Ruiz-Trejo, Solid State Ionics 181 (2010) 1349–1354.
[49] S. Lazure, Ch. Vernochet, R.N. Vannier, G. Nowogrocki, G. Mairesse, Solid State Ionics 90 (1996) 117–123.
[50] C. Pirovano, M.C. Steil, E. Capoen, G. Nowogrocki, R.N. Vannier, Solid State Ionics 176 (2005) 2079–2083.
[51] S. Beg, A. Al-Alas, N.A.S. Al-Areqi, J. Alloys Compd. 493 (2010) 299–304.
[52] G.J. Brug, A.L.G. Van Den Eeden, M. Sluyters-Rehbach, J.H. Sluyters, J. Electroanal. Chem. 176 (1984) 275–295.
[53] M.S. Islam, R.A. Davies, J. Mater. Chem. 14 (2004) 86–93.
[54] F.A. Kroger, H.J. Vink, Solid State Physics, Academic press, Inc., New York, 1956.
[55] M. Kurumada, H. Hara, F. Munakata, E. Iguchi, Solid State Ionics 176 (2005) 245–251.
[56] R. Gerhardt, J. Phys. Chem. Solids 55 (1994) 1491–1506.
[57] S. Komine, F. Munakata, J. Mater. Sci. 40 (2005) 3887–3890.
[58] H. Frölich, Theory of Dielectric, Clarendon, Oxford, 1958.